Binderless zeolite LTA beads with hierarchical porosity for selective CO2 adsorption in biogas upgrading

Boer, Dina G.; Langerak, Jort; Bakker, Benny; Pescarmona, Paolo P.

Published in:
Microporous and Mesoporous Materials

DOI:
10.1016/j.micromeso.2022.112208

Publication date:
2022

Microporous and Mesoporous Materials 344 (2022) 112208

Contents lists available at ScienceDirect

Microporous and Mesoporous Materials

journal homepage: www.elsevier.com/locate/micromeso

Binderless zeolite LTA beads with hierarchical porosity for selective CO_2 adsorption in biogas upgrading

Dina G. Boer [a,b], Jort Langerak [b], Benny Bakker [b], Paolo P. Pescarmona [a,*]

[a] Chemical Engineering Group, Engineering and Technology Institute Groningen (ENTEG), Faculty of Science and Engineering, University of Groningen, Nijenborgh 4, 9747 AG Groningen, the Netherlands
[b] DMT Environmental Technology, Yndustrywei 3, 8501 SN Joure, the Netherlands

ARTICLE INFO

Keywords:
Zeolite
Adsorption
CO_2
Hierarchical porosity
Biogas upgrading

ABSTRACT

In the context of CO_2 removal from biogas, a series of binderless zeolite LTA adsorbents with a macroscopic bead format (0.5–1.0 mm) and with hierarchical porosity (i.e. with the zeolitic micropores being accessible through meso- and macropores mainly in the 10–100 nm range) was synthesized with a variety of Si/Al ratios (1.2–3.9) using Amberlite IRA-900 anion-exchange resin beads as a hard template. The CO_2 and CH_4 adsorption capacity of the beads in Na-form with different Si/Al ratios were measured, reaching higher CO_2/CH_4 selectivity and similar, yet slightly higher CO_2 adsorption compared to commercial zeolite LTA pellets containing a binder. Subsequently, one the zeolitic beads was subjected to different degrees of ion-exchange (0–96%) with KCl and then tested in the adsorption of CO_2 and CH_4. The best performance among all the ion-exchanged beads was achieved with $Na_{58}K_{42}$-LTA beads, which gave very high CO_2/CH_4 selectivity (1540). Although essentially no CH_4 was adsorbed on these beads, the CO_2 adsorption capacity was still substantial (1.9 mmol g^{-1} at 0.4 bar CO_2, i.e. the partial pressure of CO_2 in biogas).

1. Introduction

Biogas is produced through the anaerobic digestion of organic matter and consists of approximately 60 vol% CH_4 and 40 vol% CO_2 as main components [1]. The energy content of biogas is directly related to the CH_4 content. The energy content of methane, described by the Lower Calorific Value (LCV), is 36 MJ/$m^3_{CH_4}$ compared to 20 MJ/$m^3_{biogas\ (60\ vol\%\ CH_4)}$ at STP conditions [2]. By upgrading biogas through selective separation of carbon dioxide, a substitute for natural gas is obtained that can be used as a renewable fuel, for example in combined heat and power plants, or as a vehicle fuel [1]. An additional benefit of biogas upgrading and utilization is the prevention of emission of methane into the atmosphere, as methane has a global warming potential 28 times larger than carbon dioxide [3].

Among the approaches for biogas upgrading, adsorption using solid sorbents is considered an attractive separation technology because it is a straightforward process in which no liquid waste is generated. Additionally, regeneration of solid adsorbents is easier than that of liquid absorbents, because CO_2 is mainly physisorbed on solid adsorbents, whilst it is chemisorbed on liquid absorbents. Therefore, solid adsorbents typically require lower energy for regeneration [4,5].

The development of suitable materials for the selective adsorption of CO_2 from biogas is thus a strategically important field of research. Some of the most promising and widely-studied adsorbents for CO_2 adsorption are carbon-based materials, zeolites, and metal-organic frameworks (MOFs). The assets of carbon-based materials are that they have high thermal stability, are insensitive to moisture due to their hydrophobic nature, and are available at low cost [6–8]. However, they generally have a relatively weak interaction with CO_2 and, therefore, low CO_2 adsorption capacity and selectivity towards CO_2 at low pressure [9,10]. This limitation can be mitigated by nitrogen-doping of the carbon surface, thus enhancing the interaction with CO_2 molecules [11]. MOFs are highly porous materials with specific surface areas of 1000–10000 m^2/g, and have demonstrated remarkably high CO_2 adsorption capacities, with reported values up to 33.5 mmol g^{-1} (at 35 bar) [12,13]. However, such high pressures (35 bar) are not desired in biogas upgrading applications due to the high equipment cost and energy requirements [14]. These MOFs with exceptional adsorption capacity at high pressures are less suitable for application in lower pressure ranges (< 5 bar), due to their weak interaction with CO_2 [13,15,16]. Additional limitations of MOFs are the high synthesis costs and the relatively low hydrothermal stability, which poses difficulties for regeneration [17,18]. Zeolites

* Corresponding author.
E-mail address: p.p.pescarmona@rug.nl (P.P. Pescarmona).

https://doi.org/10.1016/j.micromeso.2022.112208
Received 17 May 2022; Received in revised form 25 August 2022; Accepted 1 September 2022
Available online 8 September 2022

possess moderate adsorption capacities (1–7 mmol g^{-1}) at low pressure (1 bar), and can reach extremely high selectivity towards CO_2 ($CO_2/CH_4 > 100$) [19–22]. Furthermore, they possess excellent structural stability and can be produced easily and at low costs [15,23]. One of the biggest challenges for the application of zeolites as adsorbents is the presence of water in the gas mixture, because H_2O and CO_2 compete for the same adsorption sites and zeolites with low Si/Al ratios are susceptible to hydrolysis [24–27]. However, this limitation can be overcome, also at industrial scale, by including a pre-treatment step to remove water before the gas mixture is brought in contact with the zeolite adsorbent [28]. Zeolites typically have a relatively stronger interaction with CO_2 than carbon-based materials and MOFs and, therefore, the energy required for their regeneration can be relatively high. Although each adsorbent has specific assets and shortcomings, zeolites are of particular interest for the adsorption of CO_2 from biogas due to their high stability, low cost, and the possibility to tune their physicochemical properties (e.g. pore size and organization, composition) to optimize their adsorption behaviour.

Among the zeolite framework types, zeolite A and zeolite ZK-4 have shown promising performance for biogas upgrading. Both zeolites are characterized by the LTA framework type, with the difference being the Si/Al ratio (1 for zeolite A; > 1 for zeolite ZK-4). The LTA framework possesses a supercage which is accessible through 8 membered rings (8 MRs) with apertures of 0.3–0.5 nm, depending on the size and charge of the extra-framework cations [29]. The synthesis of zeolite A and ZK-4 yields the material in the Na-form, with apertures of about 0.4 nm, and these can be adjusted by post-synthesis ion-exchange. This means that the adsorption behaviour can be optimized by tuning the type and degree of ion-exchange [30]. Particularly, high CO_2 selectivity can be achieved by choosing the extra-framework cations such that the size of the pore aperture is in between the kinetic diameter of CO_2 (3.3 Å) and CH_4 (3.8 Å). Bacsik et al. [22] partially exchanged zeolite NaA with K^+, and through this pore size reduction, nearly no CH_4 was adsorbed whilst the CO_2 adsorption was only slightly reduced (in %). This led to a CO_2/CH_4 selectivity of > 100 at 1 bar. Cheung et al. [21] not only incorporated K^+, but also Cs^+, which even further reduced the CH_4 adsorption resulting in a CO_2/CH_4 selectivity of > 1500 at 0.5 bar CO_2 and 0.5 bar CH_4. The same principle was shown for CO_2/N_2 separation, with N_2 having a kinetic diameter of 3.64 Å. Cheung et al. partially exchanged zeolite Na-ZK-4 with 26 at% K^+, and reached a CO_2/N_2 selectivity > 800 at 0.15 bar CO_2 and 0.85 bar N_2 and 273 K, indicating that essentially no N_2 was adsorbed whilst the CO_2 adsorption was still high (4.4 mmol g^{-1}) [31].

Zeolites are normally synthesized in the form of powders. This means that in order to use them in an adsorption processes, they first must be shaped into macroscopic pellets (typical size: 2–6 mm) to minimize the pressure drop over the adsorption column [32]. Typically, an inert binder material is added to the zeolite powder to form pellets with cylindrical shape or bead format. However, this decreases the adsorption capacity per gram, and there is a trade-off between high mechanical stability and facile diffusion of CO_2 through the pellets [33]. In this work, we overcome the limitations caused by the use of a binder by introducing and investigating an attractive alternative: binderless zeolite LTA beads with a macroscopic format and with hierarchical porosity. The synthesis of these zeolitic beads was achieved using an anion-exchange resin as hard template with the double role of shaping the material into a bead format and, upon removal by calcination, to generate a network of meso- and macropores providing access to the micropores of the zeolite LTA framework. This method was inspired by the work of Tosheva et al., who reported the synthesis of Silicalite-1, ZSM-5 and zeolite Beta beads [34–36], and by more recent reports on titanosilicate beads for application as oxidation catalysts [37–40], and zeolite ZK-4 beads for *n*-hexane adsorption [41]. This is the first time that a hard-templating method employing resin beads is employed for preparing LTA beads with different Si/Al ratios and that such class of materials is investigated as CO_2 adsorbents in the context of biogas upgrading, achieving promising results in terms of CO_2/CH_4 selectivity. Our method differs significantly from emulsion-based sol-gel processing method that have been reported for preparing SiO_2 [42–44] or zeolitic [45] microspheres and from a method that uses metakaolin as a temporary binder, which after granulation to form beads is hydrothermally converted into a zeolite LTA phase [46,47]. Additionally, the resin beads employed as hard template in our work are commercially available and inexpensive (ca. 8 €/kg for bulk orders in 2020), which represents an asset in view of a potential upscaled production of these novel CO_2 adsorbents.

2. Experimental

2.1. Materials

Amberlite IRA-900 in chloride form (particle size 650–820 μm), Ludox HS-40 colloidal silica (40 wt% in H_2O), potassium chloride (KCl, ≥ 99%), silica gel (SiO_2, high purity grade, 230–400 mesh particle size), sodium aluminate ($NaAlO_2$), sodium metasilicate (Na_2SiO_3, 50–53% SiO_2), and tetramethylammonium hydroxide (TMAOH, 25 wt% in H_2O) were purchased from Sigma-Aldrich. Sodium hydroxide (NaOH, 98%) was purchased from Boom. Zeolite 4A beads were obtained from Luoyang Jalon Micro-Nano New Materials Co. Ltd. H_2O used in this work was always MilliQ grade.

2.2. Synthesis of the zeolitic beads

In Table 1, an overview is given of the synthesis parameters used in the preparation of the four zeolite bead samples. The amount of chemicals used and the ageing and crystallization times differ between the zeolites, but the general procedure is the same in all cases. The method is based on an original ZK-4 synthesis protocol from the IZA database of verified zeolite synthesis methods [48]. The synthesis of zeolite LTA-B1 (with bead format) is described in detail below.

14.65 g of deionized H_2O was added to a 100 ml beaker, after which 0.30 g NaOH and 2.15 g $NaAlO_2$ were added subsequently. The resulting solution was stirred using a magnetic bar at 500 rpm for 2h. 29.20 g TMAOH aqueous solution (25 wt%) and 1.71 g H_2O were added to the Teflon liner of a 100 ml stainless steel autoclave. 2.28 g SiO_2 (silica gel) was subsequently added to the Teflon liner and the suspension was stirred at 500 rpm for 2 h. After both mixtures had been stirred for 2h, the aluminate solution was added to the silicate suspension, and the resulting silicoaluminate mixture was stirred at 500 rpm for 1 h. 2.20 g Amberlite IRA-900 was added to the silicoaluminate mixture. After mixing for 1 min, the autoclave was closed and the reaction mixture was aged statically at room temperature for 72 h. The autoclave was then placed into an oven for the static hydrothermal crystallization at 100 °C for 72 h. After cooling down to room temperature, the product was filtered over a Büchner funnel and washed with 1 L of deionized H_2O. This procedure yielded the desired beads and a powder-fraction side product. After drying overnight at room temperature, the beads were separated from the powder fraction by sieving. The beads and the powders were calcined using the following programme: heating 3 °C/min to 200 °C, 6 h at 200 °C, heating 2 °C/min to 600 °C, 6 h at 600 °C. The yield of the beads is given in Table 1.

The synthesis of zeolite LTA-B1 was repeated on a larger scale (LTA-B1b), by employing a 500 ml stainless steel autoclave with a Teflon liner insert. For the washing step, 3 L of deionized H_2O was used. The yield of the beads is given in Table 1.

The molar composition in the reaction mixtures was:

LTA-B1 1 Al_2O_3: 2.9 SiO_2: 1.3 Na_2O: 6.1 TMAOH: 162 H_2O

LTA-B1b 1 Al_2O_3: 2.9 SiO_2: 1.3 Na_2O: 6.1 TMAOH: 162 H_2O

LTA-B2 1 Al_2O_3: 6.5 SiO_2: 1.6 Na_2O: 5.2 TMAOH: 218 H_2O

Table 1
Overview of synthesis parameters for zeolite LTA-B1 to LTA-B4.

	H_2O (g)	NaOH (g)	$NaAlO_2$ (g)	+	TMAOH (25 wt%) (g)	H_2O (g)	SiO_2 (g)	Amberlite (g)	Ageing (h)	Crystallization time (h)	Si/Al ratio in the reaction mixture	Yield (g)
LTA-B1	14.7	0.3	2.2		29.2	1.7	2.3	2.2	72	72	1.45	0.68
LTA-B1b	61.5	1.3	9.0		122.6	7.2	9.5	9.2	96	96	1.45	2.08
LTA-B2	29.3	0.6	2.2		25.0	3.4	5.1	2.2	72	72	3.26	0.47
LTA-B3	29.3	0.6	2.2		20.0	3.4	5.1	2.0	72	72	3.26	0.41
LTA-B4	12.5	3.2	2.4		–	27.7	2.4	2.4	24	72	1.39	0.44

LTA-B3 1 Al_2O_3: 6.5 SiO_2: 1.6 Na_2O: 4.2 TMAOH: 203 H_2O

LTA-B4 1 Al_2O_3: 2.8 SiO_2: 3.8 Na_2O: 158 H_2O

A mass ratio in the range 20:1 to 30:1 between the reaction mixture and the Amberlite resin beads used as hard template was found to be optimal in the synthesis of the zeolitic beads (data for mass ratios outside the optimum interval are not shown). In this optimum range, nearly all Amberlite beads are filled and covered by a shell of zeolitic matter (Fig. 1 for microscopy images of LTA-B1; Figure S1 for those of the pristine Amberlite beads and Figure S2 for those of all other beads) and good crystallinity in the beads can be obtained. Increasing the amount of template beads in the reaction mixture can lead to partially or completely empty Amberlite beads or to a decrease in crystallinity.

2.3. Synthesis of zeolite powder

Zeolite A in powder format (LTA-P1) was synthesized following a method from the IZA database of verified zeolite synthesis procedures [49], by employing half of the amounts compared to the original synthesis method. The synthesis was performed in a 100 ml polypropylene bottle. Na_2SiO_3 and $NaAlO_2$ were used as Si and Al source, respectively. NaOH was used as a base. The molar composition in the reaction mixture was 1 Al_2O_3: 1.4 SiO_2: 2.6 Na_2O: 88 H_2O. The final yield was 2.9 g.

2.4. Ion-exchange of the zeolitic beads

The zeolite LTA-B1b beads (in their original Na-form) were partially ion-exchanged, which gave a series of beads with potassium content (determined by XRF and reported as $K^+/(Na^+ + K^+)$) ranging from 0 to 96% (Table 2). For each ion-exchange procedure, zeolite LTA-B1b was added to a solution of deionized H_2O and KCl and the mixture was stirred for 30 min, 400 rpm at room temperature (see Table 2 for the detailed reaction conditions). The stirring was performed by means of an overhead stirrer because agitation with a stirring bar may damage the zeolitic beads. After stirring for 30 min, the sample was washed with deionized H_2O and dried overnight at room temperature. For preparing the LTA-B1b-96 sample, a second cycle of ion-exchange with the same reaction conditions was performed.

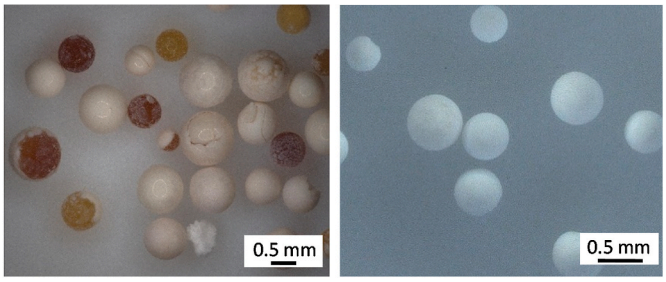

Fig. 1. Digital microscopy image of the LTA-B1 beads before calcination (left) and after calcination (right). For most uncalcined beads, a shell of zeolitic matter (white) is formed around the resin bead (yellow/orange). See Fig. S1 for a digital microscopy image of the Amberlite resin used as a hard template. (For interpretation of the references to colour in this figure legend, the reader is referred to the Web version of this article.)

Table 2
Reaction conditions for the ion-exchange of zeolite LTA-B1b beads.

	LTA-B1b (g)	H_2O (g)	KCl (g)	[KCl] (M)	$\%K^+$
LTA-B1b	–	–	–	–	0
LTA-B1b-13	0.25	12.5	0.0074	0.008	13
LTA-B1b-21	0.25	12.5	0.015	0.016	21
LTA-B1b-28	0.25	12.5	0.027	0.029	28
LTA-B1b-42	0.5	25	0.10	0.053	42
LTA-B1b-55	0.5	25	0.19	0.10	55
LTA-B1b-64	0.25	12.5	0.19	0.20	64
LTA-B1b-74	0.25	12.5	0.38	0.41	74
LTA-B1b-88	0.25[a]	12.5	0.75	0.81	88
LTA-B1b-96	0.25[b]	12.5	0.75	0.81	96

[a] The starting material was LTA-B1b-55 instead of LTA-B1b.
[b] The starting material was LTA-B1b-42 instead of LTA-B1b; for this sample, two ion-exchange cycles at the provided conditions were carried out.

2.5. Characterization

Powder X-ray diffraction (PXRD) measurements were carried out on a Bruker D8 Advance diffractometer with Cu Kα1 radiation (λ = 1.5418 Å) under 40 kV and 40 mA in the range 5–60° with a step size of 0.02°. Prior to the PXRD measurements, the beads were ground to a powder using a mortar and pestle. The slit-width was 2 mm. Elemental analysis was performed using X-ray fluorescence (XRF) measurements on an Epsilon 3^{XLE} spectrometer from PANalytical. The samples (powders or beads) were placed in a plastic cup with 6 μm mylar film. Quantification was done using the fundamental parameters method. The elements were determined assuming that they were in their oxide form and the sum of the obtained concentrations was normalized to 100%. Nitrogen physisorption measurements were performed on a Micromeritics ASAP 2420 machine at −196 °C. The specific surface area was calculated using the Brunauer-Emmet-Teller (BET) method. The pore size distribution and the meso- and macropore volume were calculated using the Barrett-Joyner-Halenda (BJH) model (from the desorption branch). The micropore volume was calculated using the t-Plot method. It should be noted that the Na^+ cations in the unit cell of zeolite LTA have been reported to limit the accessibility of the zeolite micropores to N_2, which means that for zeolite A (i.e. LTA with Si/Al = 1) the specific surface area and micropore volume assessed by N_2 physisorption are expected to be very low, whereas for zeolite ZK-4 (Si/Al > 1, and thus lower Na-content), larger values have been observed [50]. A VHX-7000 Keyence digital microscope was used to determine the average bead size, by measuring a random set of 40 beads. The obtained bead size was reported as average diameter (mm) ± standard deviation (mm). The surface morphology of the beads was determined using scanning electron microscopy (SEM) on a FEI NovaNano SEM 650 apparatus. Mechanical strength measurements of selected beads were carried out on an Instron 4301 compression tester with a maximum load of 1 kN (for the LTA-B1b and the commercial 4A beads) and an Instron 4301 compression tester with a maximum load of 5 kN (for the commercial 4A beads). For each test, a stainless steel holder (in which the piston exerting the force fits exactly) was filled with a small bed of adsorbent. The piston crushes the bed (speed 2 mm min^{-1}) until it reaches the maximum load (1 kN or 5 kN). The mechanical strength of the bed is determined by dividing the

load at breakage by the surface area of the bed (see Supplementary Information for further details). CO_2 and CH_4 adsorption tests were carried out at room temperature (24 °C) on a Micromeritics ASAP 2020 apparatus. Prior to the tests, the samples were degassed under vacuum at 350 °C for 10 h to eliminate H_2O and other possible adsorbates.

3. Results and discussion

With the purpose of developing novel, binderless zeolitic adsorbents with hierarchical porosity, a set of zeolitic beads (LTA-B1 – LTA-B4) was synthesized using a new hard-templating method developed by adapting previously reported protocols for the synthesis of LTA zeolites in powder format [48]. The obtained zeolitic beads were characterized by a combination of techniques (XRD, SEM, XRF, N_2 physisorption) and compared with a zeolite LTA powder (LTA-P1). Their applicability for CO_2 adsorption in the context of biogas upgrading was investigated and the most promising beads were ion-exchanged in order to improve their performance in terms of CO_2/CH_4 selectivity.

3.1. Synthesis and characterization of the zeolitic beads

The zeolitic beads were synthesized utilizing Amberlite IRA-900, a meso- and macroporous anion-exchange resin with a bead format [51], as hard template with two roles: (i) shaping the zeolitic material into macroscopic bead format and (ii) generating a network of meso- and macropores connecting the zeolite crystallites that constitute the beads (Fig. 2). It is proposed that negatively charged zeolitic oligomers are formed in the basic reaction solution [39]. After adding the resin beads to the reaction mixture, the anions in the resin beads are exchanged with these oligomers. Hydrothermal crystallization of these oligomers yields polymer beads filled with interconnected zeolite particles. Not all the oligomers present in the reaction mixture enter the beads: the hydrothermal crystallization of the oligomers that remain in solution yields zeolite particles in powder form as side product. The bead fraction was then calcined to remove the polymer template, yielding binderless zeolitic beads, which are expected to present an interconnected hierarchical porous structure in which the meso- and macropores generated by burning off the polymer provide access to the micropores of the zeolite crystals (Fig. 2).

A set of four different binderless zeolitic beads was prepared according to this methodology, by varying the parameters that were expected to exert a significant influence on the formation of the zeolites, i.e. the amount of chemicals that were used in the synthesis, as well as the ageing and crystallization times (Table 1). All syntheses yielded zeolite LTA beads, but the physicochemical properties of the beads differed, which in turn is anticipated to influence their performance as adsorbents. Although a bead format with a size in the range 0.49–0.97 mm was obtained in all syntheses (Table 3), SEM analysis indicated a different degree of structural integrity, with the LTA-B1 materials displaying a well-defined, intact bead format (Fig. 3A), whereas the LTA-B2 and LTA-B3 beads were more fragile and some of them would get damaged (Fig. 3D and F) by pressing them with a spatula against the carbon tape used as support for SEM measurements. The LTA-B4 beads were the most fragile of the set, and a significant fraction of them were found to present a less well defined, deformed spherical shape and to display imperfections or damages (Fig. 3I and Figure S2). Despite these differences at the macroscopic level, XRD analysis demonstrated that all the beads displayed crystallinity, showing the characteristic peaks corresponding to the LTA framework (Fig. 4). Additionally, all the diffractograms presented a broad peak with relatively low intensity centred at ~23°, which indicates the presence of amorphous silica or aluminosilicate in the beads (see also Figures S3–S6). Deconvolution of the XRD patterns allowed estimating the degree of crystallinity of the zeolitic beads (Table 3, Figure S7 and S8, explanation of the applied method in SI). The ratio of the peaks originating from the LTA framework to the broad peak corresponding to amorphous silica/aluminosilicates is highest in the LTA-B4 beads, which thus possess superior degree of crystallinity (79%) compared to the other beads. In agreement with the XRD results, SEM images with higher magnification clearly showed the presence of the zeolite crystals that constitute the beads, with LTA-B4 displaying the most defined cubic crystals with size up to 10 μm (Fig. 3K). In line with expectations, all the beads contain a large amount of mesopores and macropores in the form of structural voids between the zeolite crystals, as it can clearly be seen in Fig. 3C, E, Fig. 3H, K. An additional feature that was observed by SEM is the presence of a shell that can completely or only partly cover the surface of the beads (Fig. 3A and B). This shell is most likely amorphous and is present in beads LTA-B1–LTA-B3, whereas it is only observed in a few LTA-B4 beads (Fig. 3I). We hypothesize that the lack of such an amorphous shell could be the reason for the observed lower structural stability of the LTA-B4 beads.

The Si/Al ratio is an important feature in determining the CO_2 adsorption behaviour of a zeolite. The presence of Al (oxidation state +3) instead of Si (+4) in an aluminosilicate zeolite leads to a negatively charged framework, which needs to be balanced by extra-framework cations (typically Na^+). In zeolites with a lower Si/Al ratio (i.e. with a higher content of Al in the framework), a higher number of Na^+ cations is present per gram of material (and thus a lower Si/Na, see Table 4). These Na^+ cations are the active sites for the adsorption of CO_2 in LTA zeolites [52,53]. Therefore, a lower Si/Al ratio is expected to give a higher CO_2 adsorption capacity. The different syntheses yielded beads

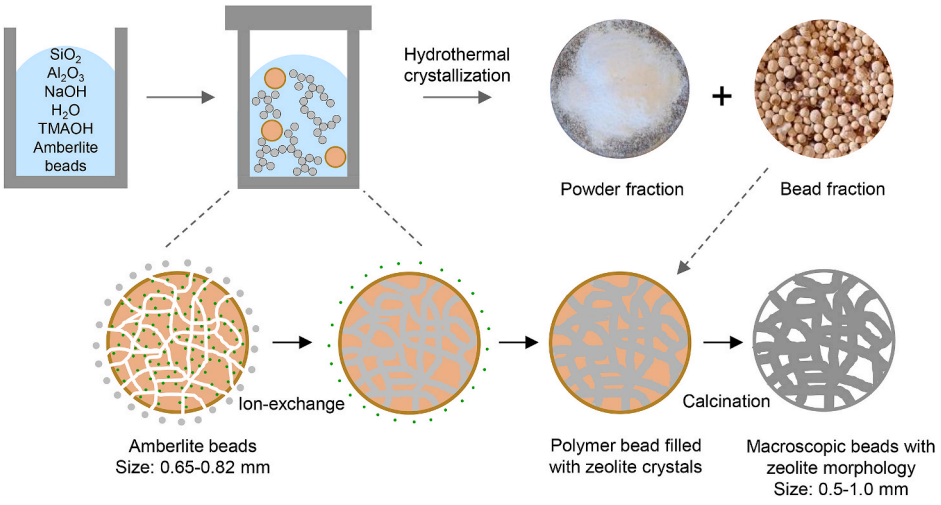

Fig. 2. Proposed synthesis route of binderless zeolitic beads using an anion-exchange resin template.

Table 3
Yields of the zeolitic beads and the crystalline phase of the beads and the corresponding side product.

Sample	Yield beads (g)	Yield powder (g)	Bead size (mm)	Reaction mixture: hard template mass ratio	Crystalline phase of the beads	Degree of crystallinity (%)	Crystalline phase of the powder side product
LTA-B1	0.68	2.3	0.77 ± 0.13	23:1	LTA	75	LTA + trace FAU
LTA-B2	0.47	2.5	0.73 ± 0.11	30:1	LTA	64	SOD + trace LTA
LTA-B3	0.41	3.8	0.60 ± 0.11	30:1	LTA	52	CHA + LTA + SOD
LTA-B4	0.44	3.3	0.81 ± 0.16	20:1	LTA	79	LTA + FAU
LTA-B1b	2.08	11.5	0.82 ± 0.12	23:1	LTA	75	LTA

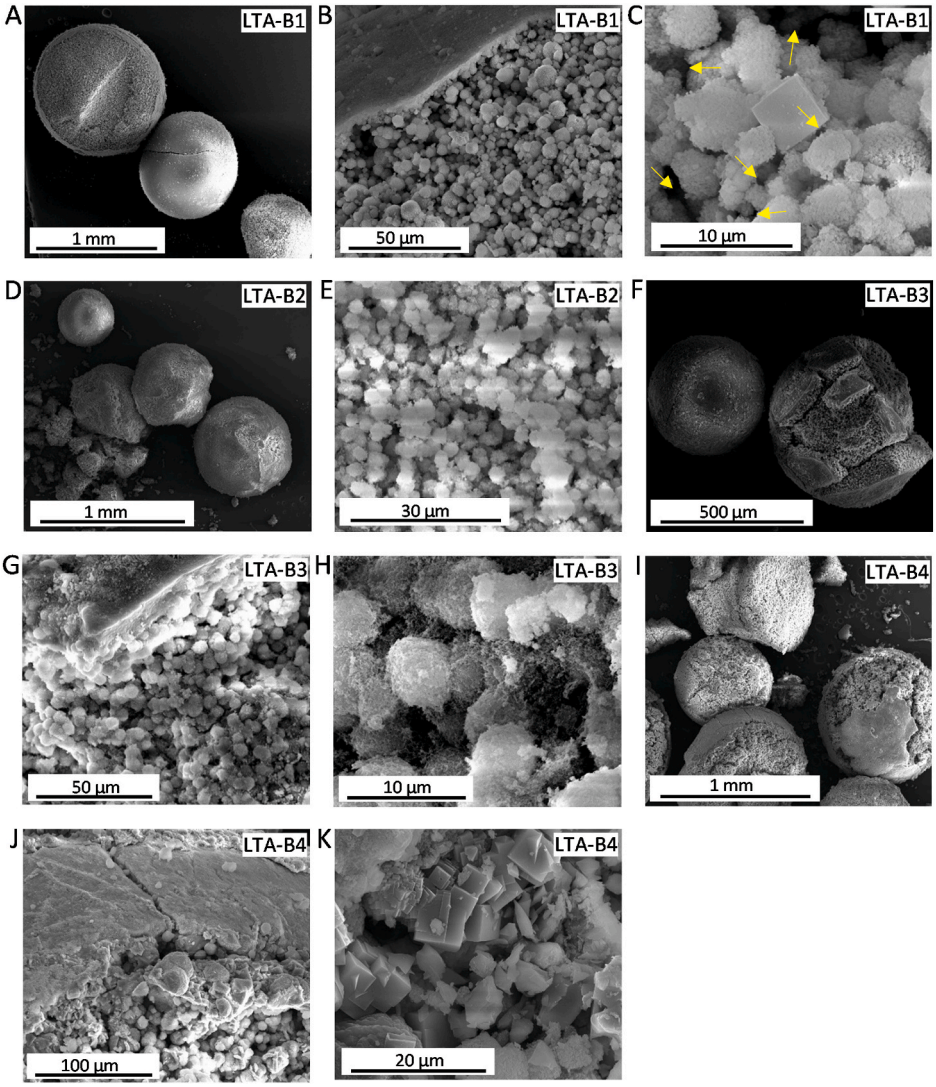

Fig. 3. SEM images of the zeolitic beads LTA-B1, LTA-B2, LTA-B3, and LTA-B4.

with a range of Si/Al ratios, as determined by XRF (full chemical composition in Table S1). Zeolite A has Si/Al = 1, whereas for higher Si/Al ratios the material should be referred to as zeolite ZK-4. Based on the XRF analysis (Table 4), it was found that the zeolitic beads have a Si/Al ratio between 1.2 (LTA-B4) and 3.9 (LTA-B3) and, therefore, it can be inferred that all the beads (LTA-B1 – LTA-B4) consist of zeolite ZK-4. However, it must be noted that the measured Si/Al ratio is the value of the whole beads and because these also contain an amorphous phase, the zeolitic domains do not necessarily have the same Si/Al ratio as the whole material. The fact that the synthesis of the LTA-B2 and LTA-B3 beads only differ in the amount of TMAOH used (higher for LTA-B2) and that the obtained materials have similar morphology but significantly different Si/Al (2.31 for LTA-B2 vs. 3.91 for LTA-B3) suggests that the higher concentration of OH^- in solution facilitated the incorporation of Al in the material. It is worth noting that a correlation was observed between the degree of crystallinity and the Si/Al ratio of the beads (Figure S9), with higher crystallinity being associated with a lower Si/Al, which might indicate that the amorphous phase is richer in Si compared to the zeolitic domains.

The pore volume and specific surface area of the prepared materials were investigated by N_2 physisorption (Table 4). The N_2 adsorption isotherms of the beads (LTA-B1 - LTA-B4, see Fig. 5) all show a hysteresis at higher relative pressure ($p/p^0 = 0.6–1$), which indicates the presence of meso- and/or macropores. The pore size distribution is broad

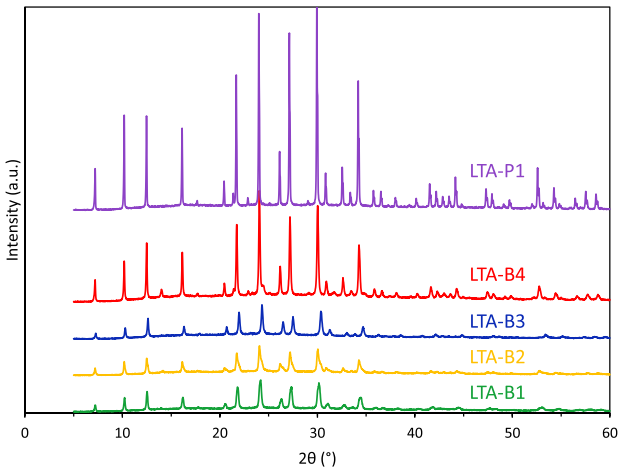

Fig. 4. XRD patterns of LTA-B1, LTA-B2, LTA-B3, LTA-B4 and LTA-P1.

(10–100 nm, see Figure S10) and covers both the mesopore and macropore range. Combining the pore size distribution obtained from the N_2 physisorption results with the SEM images, we can conclude that the desired hierarchically porous structure was obtained for the LTA-B1 – LTA-B4 beads, in which the micropores in the zeolite crystals are accessible through the network of meso- and macropores present within the beads. This hierarchical configuration of the pores is expected to facilitate the diffusion of CO_2 into the beads. The meso- and macropore volume differs significantly among the beads (Table 4), showing an increasing trend in meso- and macropore volume with decreasing crystallinity of the beads. This suggests that the amorphous phase contributes in generating and/or preserving the meso- and macropores. While the N_2 physisorption data are useful to estimate the mesopores present in our beads, care should be taken in the analysis of the zeolitic micropores and of the specific surface area. The reason for this is that N_2 has been reported to experience diffusion limitations through the narrow pore mouth of zeolite A (i.e. LTA with Si/Al = 1) in Na-form, leading to extremely low BET surface area and micropore volume [50]. This effect is correlated to the amount of Na^+ cations present in the framework, which cause a decrease in the available micropore volume. Zeolite ZK-4 (i.e. LTA with Si/Al > 1) contains less Na^+ cations in the pores per unit cell compared to zeolite A, making the effective pore size comparatively larger. Therefore, it has been shown that for LTA zeolites with lower Na-content (Si/Al ≥ 1.9) the surface area and micropore volume assessed by N_2 physisorption are much higher than for zeolite A [50] and are in the typical range observed for zeolite frameworks. In line with these previous findings, we observed a decreasing trend in specific surface area and micropore volume with increasing Na-content in our beads (Fig. 6). An analogous trend is observed with increasing Al-content, and thus with decreasing Si/Al. The adsorption isotherms for LTA-B1, LTA-B2 and LTA-B3 show a sharp increase below $p/p^0 = 0.05$ (Fig. 5), indicative of the presence of micropores, whereas the adsorption isotherms for LTA-B4, which are the beads with the highest Na-content and lowest Si/Al ratio, does not show such behaviour, leading to a very low micropore volume (Table 4). The remarkably low surface area and pore volume of LTA-B4 are probably not only caused by the higher number of Na^+ cations per unit cell, but also by the larger size of the zeolite crystals that constitute this material (as shown by SEM, *vide supra*), which implies that a larger fraction of the microporous structure will experience the diffusion limitations caused by the large amount of Na^+ cations in the material. The beads with the lowest Na-content and highest Si/Al ratio (LTA-B3), displayed the largest

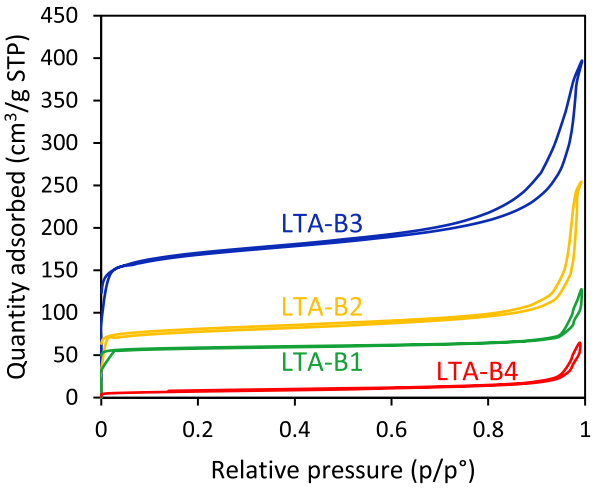

Fig. 5. N_2 physisorption isotherms of LTA-B1, LTA-B2, LTA-B3, and LTA-B4.

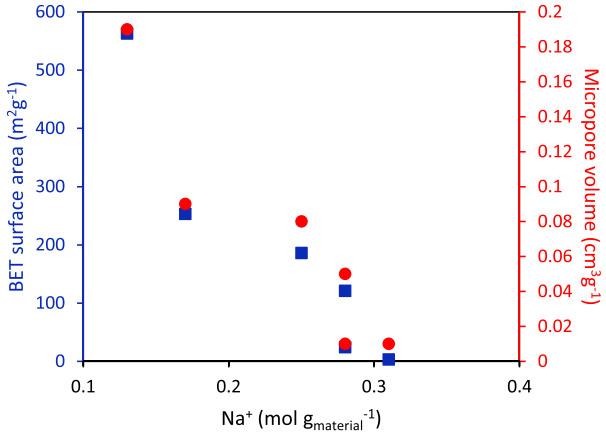

Fig. 6. BET surface area and micropore volume as a function of the amount of Na^+-sites for the zeolite LTA beads (LTA-B1, LTA-B1b, LTA-B2, LTA-B3, and LTA-B4) and for the LTA zeolite in powder form (LTA-P1).

Table 4
Physicochemical properties of the zeolitic beads LTA-B1 to LTA-B4.

Sample	BET surface area ($m^2\ g^{-1}$)	Micropore volume ($cm^3\ g^{-1}$)	Meso- and macropore volume ($cm^3\ g^{-1}$)[a]	Si/Al[b]	Si/Na[b]	Na/Al[b]	Na^+ (mol g_{bead}^{-1})[b]
LTA-B1	186	0.08	0.11	1.45	1.69	0.86	0.25
LTA-B2	253	0.09	0.29	2.31	3.05	0.76	0.17
LTA-B3	563	0.19	0.40	3.91	4.58	0.85	0.13
LTA-B4	24	<0.01	0.09	1.21	1.35	0.90	0.28
LTA-P1	3	<0.01	<0.01	1.05	1.18	0.85	0.31

[a] Determined with the BJH method.
[b] Determined by XRF analysis.

surface area (563 $m^2\ g^{-1}$) and micropore volume (0.19 $cm^3\ g^{-1}$), with the former being very similar and the latter being lower compared to those reported in the literature for ZK-4 zeolites with Si/Al ≥ 1.9 [50]. It is worth noting that the surface area and micropore volume of LTA-B2 (Si/Al = 2.31) are markedly lower than those of a zeolite ZK-4 (in powder form) with Si/Al = 1.9 reported in the literature [50]. This is in line with our above-mentioned hypothesis that the zeolitic domains of our beads have a higher Al content and thus a lower Si/Al compared to that of the whole material, and that the amorphous phase is richer in Si compared to the zeolitic phase.

The yield of the beads and of the zeolites in powder form that were obtained as side product are shown in Table 3 (see Table S2 for the chemical composition of these powders and Table S3 for their Si/Al ratio). The yield of the beads varies between 10 and 23% of the total yield. The powder product formed during the synthesis of the LTA-B1 beads consisted of LTA zeolite with small amounts of FAU zeolite (Figure S11). On the other hand, the powder product that was formed during the synthesis of LTA-B4 consisted mainly of FAU zeolite with small amounts of LTA zeolite (Figure S12). The powder product obtained during the preparation of the LTA-B2 beads consisted mainly of SOD zeolite mixed with trace amounts of LTA zeolite (Figure S13). Finally, the powder obtained together with the LTA-B3 beads is less valuable because it consisted of a mixture of zeolites (CHA + LTA + SOD + other unknown peaks) (Figure S14).

The synthesis of zeolite beads LTA-B1 was repeated at a larger scale (LTA-B1b), leading to a comparable material in terms of features of the bead (see SEM images, XRD pattern and N_2 physisorption data, Figures S15-S17, Table S4), and thus proving the upscalability (by a factor 4) of our synthesis method. The powder product obtained together with the LTA-B1b beads was pure LTA zeolite powder and is therefore also a valuable product (Figure S18). Yet, future work should aim at optimizing the yield of the beads fraction compared to the powder one, particularly in the perspective of a potential large-scale application. Additionally, we prepared LTA in powder form (LTA-P1) as reference material, following a verified literature procedure [49]. The highly crystalline powder (see XRD pattern in Figure S19 and SEM image in Figure S20) possessed a Si/Al ratio of 1.05 and, therefore, can be considered to be zeolite A (whilst the beads all possess Si/Al > 1). Due to its low Si/Al ratio and, therefore, high amount of Na^+ cations, N_2 is not able to access most of the micropores resulting in a very low BET surface area and almost no available micropore volume for LTA-P1 (Figure S21, Table 4).

Since the LTA-B1 and LTA-B1b beads displayed the most intact bead format, the mechanical strength of a bed of LTA-B1b beads was determined by means of a compression test and compared to that of the commercial zeolite 4A beads. As anticipated, the measurements show that the mechanical strength of the beads (0.14–0.82 MPa, see Table S5 and Figures S22-S24 for further information) is lower than that of commercial binder-containing beads (1.6–18.4 MPa). Yet, based on a calculation of the pressure exerted by a bed of beads in an industrial-scale adsorption column (height: 3 m, diameter: 1 m, see SI for details), we estimated that the mechanical strength of the LTA-B1 beads should be sufficient for being used for this application without significant structural deterioration.

3.2. Application of the zeolitic beads as adsorbents for CO_2

In order to estimate the potential of the prepared zeolite LTA beads in biogas upgrading, we measured the CO_2 and CH_4 adsorption capacities for all the binderless zeolite bead samples and for commercial zeolite 4A beads (containing a binder) at room temperature in the 0–1 bar range (Fig. 7 and Table 5). The CO_2 adsorption capacities of all the synthesized zeolitic beads were comparable to that of the commercial beads, and in the case of the LTA-B2 beads a slightly higher CO_2 adsorption was achieved (3.8 $mmol_{CO_2}\ g^{-1}_{bead}$ at 1.0 bar CO_2, 3.4 $mmol_{CO_2}\ g^{-1}_{bead}$ at 0.4 bar CO_2, i.e. the partial pressure of carbon dioxide in biogas, see Table 5). The observed trend for the CO_2 adsorption capacity (LTA-P1 > LTA-B2 > 4A commercial > LTA-B1b ~ LTAB1 ~ LTA-B3 > LTA-B4) is the same at 1.0 bar and at 0.4 bar. Although the adsorption capacities of all the binderless zeolitic beads are in a similar range, they do display clear differences as it is expected considering their differences in terms of degree of crystallinity, Na-content, and of accessible micropore volume and specific surface area (Table 4). Since LTA-B2 and LTA-B3 exhibit a higher Si/Al and Si/Na ratio and a lower degree of crystallinity than LTA-B1, their amount of Na^+/g_{bead} in the zeolitic microporous structure acting as adsorption sites for CO_2 is lower. However, our results indicate that the number of adsorption sites is not the only important factor in determining the CO_2 adsorption capacity. Indeed, LTA-B3, with the lowest Na-content (0.13 mol g^{-1}_{bead}) and the lowest degree of crystallinity (52%), had a similar adsorption capacity to LTA-B1, which has the second highest Na-content (0.25 mol g^{-1}_{bead}) and the second highest degree of crystallinity (75%). The highest adsorption capacity was achieved with LTA-B2, which has an intermediate Na-content (0.17 mol g^{-1}_{bead}) and degree of crystallinity (64%) among our beads. The LTA-B4 beads displayed the highest degree of crystallinity (79%) and the largest Na-content (0.28 mol g^{-1}_{bead}), and yet had the lowest CO_2 adsorption capacity. This is ascribed to the much lower accessible micropore volume and surface area displayed by this material (Table 4). It should be noted that these textural properties were measured by N_2 adsorption, and that the kinetic diameter of CO_2 (3.3 Å) is only slightly smaller than that of N_2 (3.6 Å). This implies that CO_2 is also expected to experience diffusion limitations in the micropores of this material, though to a lower extent than N_2. Therefore, the trends in accessible micropore volume and surface area measured by N_2 physisorption are expected to be useful for interpreting the CO_2 adsorption behaviour. This set of results shows that there is a trade-off between the Na-content and the degree of crystallinity, and thus the number of adsorption sites of the zeolitic beads, which increase with decreasing Si/Al ratio in the material, and the available micropore volume and surface area, which follow the opposite trend as a function of the Si/Al ratio (*vide supra*). It is thus not surprising that the best CO_2 adsorption capacity was obtained with a material having intermediate Na-content, intermediate degree of crystallinity and intermediate micropore volume and surface area (i.e. LTA-B2). The complex interplay between these different factors is further demonstrated by the results obtained with the powder sample LTA-P1, which had the highest Na-content (0.31 mol g^{-1}_{bead}) but also the lowest accessible micropore volume, and yet the highest adsorption capacity (Table 4, Table 5). This can be ascribed to its higher degree of crystallinity compared to the beads, which implies well-defined adsorption sites. Although XRD analysis showed that the beads are largely crystalline, a fraction of amorphous material was present in all our samples (*vide supra*). On the other hand, the powder LTA-P1 was highly crystalline and did not show the presence of a detectable amount of amorphous silica/aluminosilicates (Figure S19). In order to evaluate further the effect of the degree of crystallinity of the beads on their CO_2 adsorption capacity, we chose a systematic approach and synthesized a new set of zeolite LTA beads (LTA-B5, LTA-B6 and LTA-B7, chemical composition in Table S6) using exactly the same synthesis method and amounts of chemicals, with the only difference being the ageing and crystallization times (synthesis methods in SI). These three beads were compared in terms of crystallinity (XRD, Figures S25-27 and Table S7), Na-content, surface area and micropore volume (Table S7) and CO_2 adsorption capacity (Fig. 8) with a powder (LTA-P2, XRD in Figure S28) that was synthesized with the same method, but without adding the Amberlite resin beads (synthesis method in SI). The LTA-B5 beads are partly crystalline (LTA) and partly amorphous, as indicated by the presence of the large, broad XRD peak stemming from amorphous silica/aluminosilicates from about 10 to 40°, with an estimated degree of crystallinity of 31%. The LTA-B6 beads are mostly crystalline and only show a small, broad XRD peak corresponding to the presence of amorphous material (more clearly seen in Figure S26), leading to an estimated degree of crystallinity of 62%. The LTA-B7 beads show a further

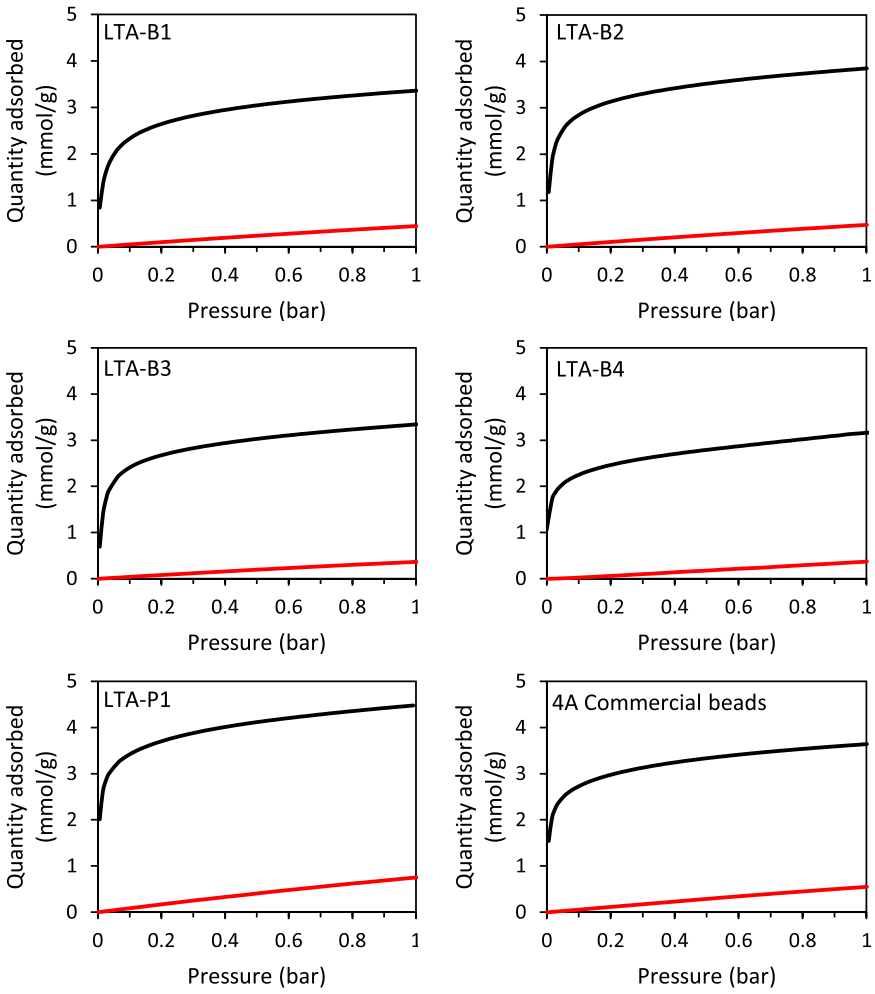

Fig. 7. CO_2 (black) and CH_4 (red) adsorption isotherms measured at room temperature for LTA-B1 to LTA-B4, LTA-P1, and for the commercial zeolite-binder beads 4A. (For interpretation of the references to colour in this figure legend, the reader is referred to the Web version of this article.)

Table 5
CO_2 and CH_4 adsorption capacity and CO_2/CH_4 selectivity for LTA-B1 to LTA-B4 beads, LTA-P1, and the commercial 4A beads.

Sample	CO_2 adsorption capacity ($mmol g^{-1}$)		CH_4 adsorption capacity ($mmol g^{-1}$)		CO_2/CH_4 selectivity[a]
	at 1.0 bar CO_2	at 0.4 bar CO_2	at 1.0 bar CH_4	at 0.6 bar CH_4	
LTA-B1	3.36	2.95	0.45	0.29	15.5
LTA-B1b	3.39	3.01	0.38	0.25	18.4
LTA-B2	3.85	3.43	0.48	0.30	17.0
LTA-B3	3.34	2.94	0.36	0.23	18.8
LTA-B4	3.16	2.82	0.37	0.22	19.4
LTA-P1	4.48	4.02	0.75	0.49	12.4
4A beads (commercial)	3.63	3.25	0.55	0.35	14.0

[a] CO_2/CH_4 selectivity calculated as Sel. $= (q_{CO_2}/q_{CH_4})/(p_{CO_2}/p_{CH_4})$, in which q_x is the adsorbed amount measured at the partial pressure p_x in the hypothetical gas mixture. To mimic biogas, the following partial pressures were used: 0.6 bar for CH_4 and 0.4 bar for CO_2.

but much less marked increase in crystallinity (65%, see also Figure S27). The observed increase in crystallinity upon increasing the ageing and crystallization times (Figures S25-S28) was correlated with a decrease in the Si/Al ratio of the beads (Table S7), similarly to what observed with LTA-B1 - LTA-B4 beads (*vide supra*). The fact that this trend was clearly observed with beads prepared with the same method provides insights in the synthesis mechanism. In the relatively crystalline LTA-B6 and LTA-B7 beads, a Si/Al = 1.3 was observed, while the partly crystalline and partly amorphous LTA-B5 beads had a Si/Al = 4.3. This suggests that a Si-rich amorphous phase is initially formed within the Amberlite beads while the Al species tend to remain in solution, and that the latter are incorporated in the material only at longer synthesis times. Within this new set of zeolitic beads, LTA-B5 displayed by far the lowest CO_2 adsorption capacity (Fig. 8). This is attributed to its low degree of crystallinity, combined with the low Na-content (Table S7). LTA-B6 and LTA-B7 presented similar features to each other in terms of degree of crystallinity, Na-content, accessible micropore volume and surface area (Table S7) and, accordingly, displayed very similar CO_2

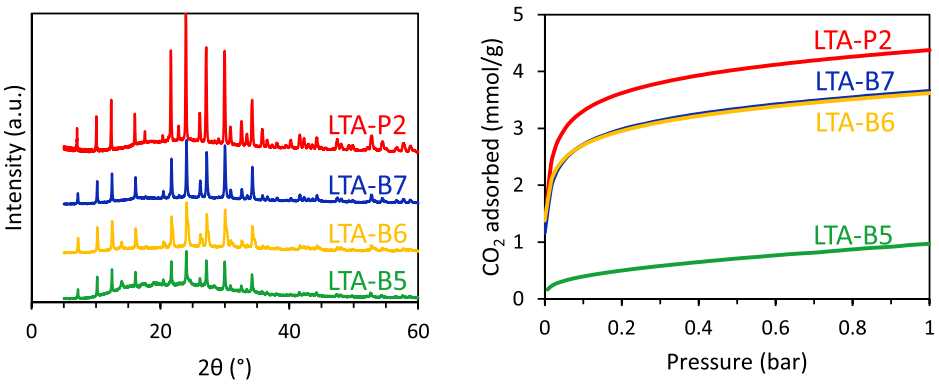

Fig. 8. XRD patterns (left) and CO_2 adsorption isotherms (right) of LTA-B5, LTA-B6, LTA-B7, and LTA-P2.

adsorption capacity (Fig. 8). The most notable result of this systematic study is the comparison between LTA-B6 and the highly crystalline LTA-P2 powder (degree of crystallinity of 84%, see also Figure S28). These two materials were prepared with the same synthesis method and are very similar in terms of Na-content, accessible micropore volume and surface area but differ significantly in the degree of crystallinity (Table S7). The higher CO_2 adsorption capacity shown by LTA-P2 compared to LTA-B6 (Fig. 8) clearly indicates that a high degree of zeolite crystallinity is favourable for the CO_2 adsorption capacity of the material.

The hierarchical structure of the beads is expected to facilitate the diffusion of CO_2 into the adsorbing material. Therefore, in the comparison between materials in bead and powder format discussed above, we assumed that the meso- and macropores of the beads were able to provide access to the microporous zeolitic structures without causing any significant mass transfer limitation. In order to check whether this was actually the case, we ground LTA-B1 and LTA-B1b into powders and measured again the CO_2 adsorption capacity (Figure S29). The fact that the two measurements took approximately the same time and that the CO_2 adsorption curves of the beads overlapped with those of the corresponding ground samples (in which the hierarchical structure is not anymore present) demonstrates that the meso- and macropores of the beads indeed allow the unhindered diffusion of CO_2.

Our zeolitic beads (LTA-B1 to B4), the commercial bead (4A) and the LTA-P1 powder sample were tested also for their CH_4 adsorption capacity (Fig. 7). There was only a small difference in CH_4 adsorption capacity between our binderless zeolitic beads. The lowest CH_4 adsorption capacity (0.22 mmol g^{-1} at p = 0.6 bar, i.e. the partial pressure of methane in biogas) was found with LTA-B4 and led to the highest CO_2/CH_4 selectivity (Table 5). On the other hand, the commercial beads and particularly the powder LTA zeolite displayed higher CH_4 adsorption capacity than the beads (0.35 and 0.49 mmol g^{-1} at p = 0.6 bar, respectively). As a consequence of their lower CH_4 adsorption capacity, our binderless beads displayed enhanced CO_2/CH_4 selectivity compared to the commercial zeolite LTA pellets prepared using a binder and to the LTA zeolite in powder form (Table 5).

3.3. Ion-exchange of the zeolitic beads

Partial ion-exchange of LTA zeolites in Na-form with K^+ cations causes a decrease in the micropore size that has been reported to drastically limit the adsorption of CH_4 while still allowing the adsorption of a significant amount of CO_2 [22]. Therefore, we selected one of our binderless zeolitic beads and subjected it to various degrees of ion-exchange with K^+, with the purpose of enhancing the CO_2/CH_4 selectivity. Among the prepared materials, the LTA-B1 beads consisted of the most intact spherical beads and have the highest mechanical stability (upon pressing them manually with a spatula) compared to LTA-B2, LTA-B3 or LTA-B4. Therefore, the synthesis of LTA-B1 was repeated at a larger scale with the aim of performing ion-exchange on one single batch of zeolitic beads. The obtained LTA-B1b sample has analogous physicochemical properties to LTA-B1 (see SEM images, XRD pattern and N_2 physisorption data, Figures S15-S17, Table S4), demonstrating the robustness of our synthesis protocol. Also the CO_2 and CH_4 adsorption capacity of the Na-form of LTA-B1b is similar to that of LTA-B1 (compare Fig. 7 and Figure S30). Then, the LTA-B1b beads were divided into 10 batches and each was subjected to a different degree of ion-exchange in the range from 0 to 96% K^+ (and thus from 100 to 4% Na^+). The ion-exchange procedure we adopted was efficient in achieving a library of zeolite LTA beads with gradually increasing K-content, as demonstrated by XRF analysis (Table 2, full chemical composition in Table S8). This library of zeolitic beads was tested for their CO_2 and CH_4 adsorption capacity.

At low K-content (up to 13%), the CH_4 adsorption capacity of the beads is unaffected compared to their counterpart in Na-form (Fig. 9). Above 13% K^+, the CH_4 adsorption capacity starts to decrease (Fig. 9), which is attributed to an increased diffusion limitation of CH_4 as a consequence of the decrease in the micropore size caused by the larger size of K^+ compared to Na^+. More specifically, it has been shown that K^+ is preferentially located in the 8 MR windows and its presence hinders the diffusion of CH_4 and CO_2 through these windows [21]. From an ion-exchange degree of 42% K^+, the diffusion of CH_4 through the 8 MRs was hindered to such a degree that essentially no CH_4 was adsorbed (Fig. 9). These results confirm the anticipated decrease in CH_4 adsorption as a function of the K-content. The ion-exchange with K^+ also

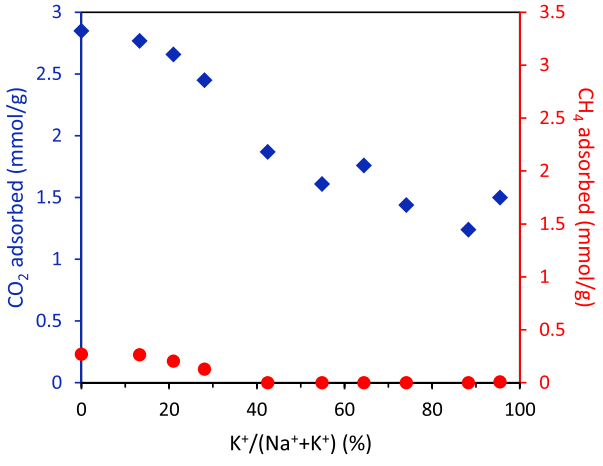

Fig. 9. CO_2 and CH_4 adsorption capacity of ion-exchanged LTA-B1b zeolitic beads at the partial pressures mimicking biogas (i.e. 0.4 bar CO_2 and 0.6 bar CH_4), as a function of K-content.

caused a noticeable decrease in CO_2 adsorption capacity, already at a K-content as low as 13% (Fig. 9). This effect can also partly be attributed to hindered diffusion through the 8 MR windows. Additionally, because K^+ is significantly larger than Na^+, the CO_2 adsorption capacity decreased due to the decreasing available micropore volume. Yet, a significant CO_2 adsorption capacity was preserved even at very high degree of ion-exchange of Na^+ with K^+. In terms of CO_2/CH_4 selectivity, an optimum was found with the zeolitic beads with a K-content of around 42%, which lead to a virtually full CO_2/CH_4 selectivity of 1540 (at the partial pressures that mimic biogas, i.e. 0.6 bar CH_4 and 0.4 bar CO_2; it should be noted that at such low degree of adsorption the quantification of CH_4 might become less accurate). At this K-content, essentially no CH_4 was adsorbed (< 0.01 mmol g^{-1} at 1.0 bar CH_4) whilst the CO_2 adsorption capacity was still substantial (2.4 mmol g^{-1} at 1.0 bar CO_2). The observed trends are in agreement with previous reports on NaK-zeolite-LTA powders [22,31]. However, in the literature the optimal K-content for maximizing the CO_2/CH_4 selectivity was found to be 27% [22]. At this K-content, the CH_4 adsorption capacity of our zeolitic beads was still 0.2 mmol g^{-1}. We propose that this difference is related to the lower Si/Al ratio of the zeolite in the literature (A type), which implies a larger population of cations (Na^+ or K^+) per unit cell and thus a general lower accessibility of the micropores of the zeolite at each K-exchange degree.

4. Conclusions

Novel hierarchically porous zeolitic beads with LTA framework and a range of Si/Al ratios (1.2–3.9) were synthesized by a hard-templating method using an inexpensive, commercially available anion-exchange resin, thoroughly characterized with a combination of techniques and then tested as adsorbents for CO_2 and CH_4. These binderless zeolitic beads in Na-form possess CO_2 adsorption capacities comparable to that of commercial zeolite 4A beads but with increased CO_2/CH_4 selectivity (up to 19.4 compared to 14.0 with the commercial 4A beads). The degree of crystallinity, the Na-content, the accessible micropore volume and specific surface area were shown to play a role in determining the CO_2 adsorption capacity of these zeolitic beads. Intermediate values of these physicochemical features were found to lead to the highest CO_2 adsorption capacity (3.85 mmol g^{-1} at 1.0 bar CO_2) as a consequence of a trade-off between the number of adsorption sites and their accessibility. Ion-exchange was used to tune the counter-cation composition of the zeolitic beads and thus enhance their CO_2/CH_4 selectivity. The optimal $K^+/(Na^+ + K^+)$ composition was around 42%, which resulted in a significantly increased CO_2/CH_4 selectivity of 1540. At this composition, essentially no CH_4 was adsorbed whilst the CO_2 adsorption selectivity was still considerable (1.9 mmol g^{-1} at 0.4 bar CO_2, i.e. the partial pressure of CO_2 in biogas, 2.4 mmol g^{-1} at 1.0 bar CO_2). In conclusion, we introduced a new class of hierarchically porous zeolitic beads that possess a favourable pore structure, which in combination with their high CO_2/CH_4 selectivity makes them attractive adsorbents for CO_2 separation from biogas. The macroscopic format of the beads and their binder-free nature are additional assets that will enable to employ them as such in an adsorption column for biogas upgrading. This work opens new perspectives for the development of selective adsorbents as the strategy of using binderless zeolitic beads for this application can be extended to other zeolite frameworks and to the separation of other gas mixtures.

CRediT authorship contribution statement

Dina G. Boer: Writing – original draft, Visualization, Validation, Methodology, Investigation, Formal analysis, Data curation. **Jort Langerak:** Supervision, Project administration, Conceptualization. **Benny Bakker:** Supervision, Project administration, Funding acquisition, Conceptualization. **Paolo P. Pescarmona:** Writing – review & editing, Supervision, Resources, Project administration, Methodology, Investigation, Funding acquisition, Formal analysis, Data curation, Conceptualization.

Declaration of competing interest

The authors declare that they have no known competing financial interests or personal relationships that could have appeared to influence the work reported in this paper.

Data availability

Data will be made available on request.

Acknowledgements

The authors acknowledge funding for the project by DMT Environmental Technology, Samenwerkingsverband Noord-Nederland (SNN, KE18PR003), and GasTerra. Léon Rohrbach is acknowledged for analytical support and Jacob Baas for support with XRD analysis and deconvolution of the XRD patterns. Stefano Poli is acknowledged for helping with the SEM analysis.

Appendix A. Supplementary data

Supplementary data to this article can be found online at https://doi.org/10.1016/j.micromeso.2022.112208.

References

[1] A. Petersson, A. Wellinger, Biogas Upgrading Technologies – Developements and Innovations, 2009.
[2] I. Angelidaki, L. Treu, P. Tsapekos, G. Luo, S. Campanaro, H. Wenzel, P.G. Kougias, Biogas upgrading and utilization: current status and perspectives, Biotechnol. Adv. 36 (2018) 452–466, https://doi.org/10.1016/j.biotechadv.2018.01.011.
[3] G. Myhre, D. Shindell, F.-M. Bréon, W. Collins, J. Fuglestvedt, J. Huang, D. Koch, J.-F. Lamaruqe, D. Lee, B. Mendoza, T. Nakajima, A. Robock, G. Stephens, T. Takemura, H. Zhang, Anthropogenic and natural radiative forcing, in: T. F. Stocker, D. Qin, G.-K. Plattner, M. Tignor, S.K. Allen, J. Boschung, A. Nauels, Y. Xia, V. Bex, P.M. Midgley (Eds.), Clim. Chang. 2013 Phys. Sci. Basis. Contrib. Work. Gr. I to Fifth Assess. Rep. Intergov. Panel Clim. Chang., Cambridge University Press, Cambridge, United Kingdom and New York, NY, USA, 2013, https://doi.org/10.3390/jmse6040146.
[4] A. Samanta, A. Zhao, G.K.H. Shimizu, P. Sarkar, R. Gupta, Post-combustion CO_2 capture using solid sorbents: a review, Ind. Eng. Chem. Res. 51 (2012) 1438–1463, https://doi.org/10.1021/ie200686q.
[5] D.Y.C. Leung, G. Caramanna, M.M. Maroto-Valer, An overview of current status of carbon dioxide capture and storage technologies, Renew. Sustain. Energy Rev. 39 (2014) 426–443, https://doi.org/10.1016/j.rser.2014.07.093.
[6] M.G. Plaza, C. Pevida, B. Arias, M.D. Casal, C.F. Martín, J. Fermoso, F. Rubiera, J. J. Pis, Different approaches for the development of low-cost CO_2 adsorbents, J. Environ. Eng. 135 (2009) 426–432, https://doi.org/10.1061/(ASCE)EE.1943-7870.0000009.
[7] A. Sayari, Y. Belmabkhout, R. Serna-Guerrero, Flue gas treatment via CO_2 adsorption, Chem. Eng. J. 171 (2011) 760–774, https://doi.org/10.1016/j.cej.2011.02.007.
[8] R. Ben-Mansour, M.A. Habib, O.E. Bamidele, M. Basha, N.A.A. Qasem, A. Peedikakkal, T. Laoui, M. Ali, Carbon capture by physical adsorption: materials, experimental investigations and numerical modeling and simulations - a review, Appl. Energy 161 (2016) 225–255, https://doi.org/10.1016/j.apenergy.2015.10.011.
[9] S. Choi, J.H. Drese, C.W. Jones, Adsorbent materials for carbon dioxide capture from large anthropogenic point sources, ChemSusChem 2 (2009) 796–854, https://doi.org/10.1002/cssc.200900036.
[10] R.V. Siriwardane, M.S. Shen, E.P. Fisher, J.A. Poston, Adsorption of CO_2 on molecular sieves and activated carbon, Energy Fuel. 15 (2001) 279–284, https://doi.org/10.1021/ef000241s.
[11] F. Sun, X. Liu, J. Gao, X. Pi, L. Wang, Z. Qu, Y. Qin, Highlighting the role of nitrogen doping in enhancing CO_2 uptake onto carbon surfaces: a combined experimental and computational analysis, J. Mater. Chem. A. 4 (2016) 18248–18252, https://doi.org/10.1039/c6ta08262a.
[12] H. Furukawa, K.E. Cordova, M. O'Keeffe, O.M. Yaghi, The chemistry and applications of metal-organic frameworks, Science 80– (2013) 341, https://doi.org/10.1126/science.1230444.
[13] A.R. Millward, O.M. Yaghi, Metal-organic frameworks with exceptionally high capacity for storage of carbon dioxide at room temperature, J. Am. Chem. Soc. 127 (2005) 17998–17999, https://doi.org/10.1021/ja0570032.

[14] M.M.F. Hasan, E.L. First, C.A. Floudas, Cost-effective CO_2 capture based on in silico screening of zeolites and process optimization, Phys. Chem. Chem. Phys. 15 (2013) 17601–17618, https://doi.org/10.1039/c3cp53627k.
[15] T.H. Bae, M.R. Hudson, J.A. Mason, W.L. Queen, J.J. Dutton, K. Sumida, K. J. Micklash, S.S. Kaye, C.M. Brown, J.R. Long, Evaluation of cation-exchanged zeolite adsorbents for post-combustion carbon dioxide capture, Energy Environ. Sci. 6 (2013) 128–138, https://doi.org/10.1039/c2ee23337a.
[16] P.A.S.S. Moura, D.P. Bezerra, D.C.S.S. Azevedo, E. Vilarrasa-Garcia, M. Bastos-Neto, D.C.S.S. Azevedo, Adsorption equilibria of CO_2 and CH_4 in cation-exchanged zeolites 13X, Adsorption 22 (2016) 71–80, https://doi.org/10.1007/s10450-015-9738-9.
[17] A.C. Kizzie, A.G. Wong-Foy, A.J. Matzger, Effect of humidity on the performance of microporous coordination polymers as adsorbents for CO_2 capture, Langmuir 27 (2011) 6368–6373, https://doi.org/10.1021/la200547k.
[18] J. Liu, P.K. Thallapally, B.P. McGrail, D.R. Brown, J. Liu, Progress in adsorption-based CO_2 capture by metal-organic frameworks, Chem. Soc. Rev. 41 (2012) 2308–2322, https://doi.org/10.1039/c1cs15221a.
[19] Q. Liu, A. Mace, Z. Bacsik, J. Sun, A. Laaksonen, N. Hedin, NaKA sorbents with high CO_2-over-N_2 selectivity and high capacity to adsorb CO_2, Chem. Commun. 46 (2010) 4502–4504, https://doi.org/10.1039/c000900h.
[20] P. Vasiliev, O. Cheung, Z. Bacsik, N. Hedin, Zeolite Type a Sorbent, US 2017/0158519 A1, 2017.
[21] O. Cheung, D. Wardecki, Highly selective uptake of carbon dioxide on the zeolite | $Na_{10.2}KCs_{0.8}$|-LTA – a possible sorbent for biogas upgrading, Phys. Chem. Chem. Phys. 18 (2016) 16080–16083, https://doi.org/10.1039/C6CP02443B.
[22] Z. Bacsik, O. Cheung, P. Vasiliev, N. Hedin, Selective separation of CO_2 and CH_4 for biogas upgrading on zeolite NaKA and SAPO-56, Appl. Energy 162 (2016) 613–621, https://doi.org/10.1016/j.apenergy.2015.10.109.
[23] P.A. Barret, N.A. Stephenson, Adsorption properties of zeolites, in: C. Martínez, J. Pérez-Pariente (Eds.), Zeolites Ordered Porous Solids Fundam. Appl., Universitat Politècnica de València, Valencia, Spain, 2011, pp. 149–179.
[24] J.A. Mason, T.M. McDonald, T.H. Bae, J.E. Bachman, K. Sumida, J.J. Dutton, S. S. Kaye, J.R. Long, Application of a high-throughput analyzer in evaluating solid adsorbents for post-combustion carbon capture via multicomponent adsorption of CO_2, N_2, and H_2O, J. Am. Chem. Soc. 137 (2015) 4787–4803, https://doi.org/10.1021/jacs.5b00838.
[25] C.J. Heard, L. Grajciar, C.M. Rice, S.M. Pugh, P. Nachtigall, S.E. Ashbrook, R. E. Morris, Fast room temperature lability of aluminosilicate zeolites, Nat. Commun. 10 (2019), https://doi.org/10.1038/s41467-019-12752-y.
[26] S. Prodinger, M.A. Derewinski, Recent progress to understand and improve zeolite stability in the aqueous medium, Petrol. Chem. 60 (2020) 420–436, https://doi.org/10.1134/S0965544120040143.
[27] B. Ray, S.R. Churipard, S.C. Peter, An overview of the materials and methodologies for CO_2 capture under humid conditions, J. Mater. Chem. A. 9 (2021) 26498–26527, https://doi.org/10.1039/d1ta08862a.
[28] K. Hoyer, C. Hulteberg, M. Svensson, J. Jernberg, Ø. Nørregård, Biogas Upgrading – Technical Review, Energiforsk, 2016.
[29] Q. Liu, A. MacE, Z. Bacsik, J. Sun, A. Laaksonen, N. Hedin, NaKA sorbents with high CO_2-over-N_2 selectivity and high capacity to adsorb CO_2, Chem. Commun. 46 (2010) 4502–4504, https://doi.org/10.1039/c000900h.
[30] A. Oda, S. Hiraki, E. Harada, I. Kobayashi, T. Ohkubo, Y. Ikemoto, T. Moriwaki, Y. Kuroda, Unprecedented CO_2 adsorption behaviour by 5A-type zeolite discovered in lower pressure region and at 300 K, J. Mater. Chem. A. 9 (2021) 7531–7545, https://doi.org/10.1039/d0ta09944a.
[31] O. Cheung, Z. Bacsik, P. Krokidas, A. Mace, A. Laaksonen, N. Hedin, K+ exchanged zeolite ZK-4 as a highly selective sorbent for CO_2, Langmuir 30 (2014) 9682–9690, https://doi.org/10.1021/la502897p.
[32] J.A.C. Silva, K. Schumann, A.E. Rodrigues, Sorption and kinetics of CO_2 and CH_4 in binderless beads of 13X zeolite, Microporous Mesoporous Mater. 158 (2012) 219–228, https://doi.org/10.1016/j.micromeso.2012.03.042.
[33] K. Schumann, B. Unger, A. Brandt, F. Scheffler, Investigation on the pore structure of binderless zeolite 13× shapes, Microporous Mesoporous Mater. 154 (2012) 119–123, https://doi.org/10.1016/j.micromeso.2011.07.015.
[34] L. Tosheva, V. Valtchev, J. Sterte, Silicalite-1 containing microspheres prepared using shape-directing macro-templates, Microporous Mesoporous Mater. 35–36 (2000) 621–629, https://doi.org/10.1016/S1387-1811(99)00256-5.
[35] L. Tosheva, J. Sterte, ZSM-5 spheres prepared by resin templating, Stud. Surf. Sci. Catal. 142 (2002) 183–190.
[36] L. Tosheva, B. Mihailova, V. Valtchev, J. Sterte, Zeolite beta spheres, Microporous Mesoporous Mater. 48 (2001) 31–37, https://doi.org/10.1016/S1387-1811(01)00327-4.
[37] K. Lin, L. Li, B.F. Sels, P.A. Jacobs, P.P. Pescarmona, Titanosilicate beads as versatile catalysts for the conversion of trioses to lactates and for the epoxidation of alkenes, Catal. Today 173 (2011) 89–94, https://doi.org/10.1016/j.cattod.2011.03.055.
[38] K. Lin, O.I. Lebedev, G. Vana Tendeloo, P.A. Jacobs, P.P. Pescarmona, Titanosilicate beads with hierarchical porosity: synthesis and application as epoxidation catalysts, Chem. Eur J. 16 (2010) 13509–13518, https://doi.org/10.1002/chem.201001508.
[39] W. Cheng, Y. Jiang, X. Xu, Y. Wang, K. Lin, P.P. Pescarmona, Easily recoverable titanosilicate zeolite beads with hierarchical porosity: preparation and application as oxidation catalysts, J. Catal. 333 (2016) 139–148, https://doi.org/10.1016/j.jcat.2015.09.017.
[40] X. Yang, Y. Jiang, Y. Li, X. Xu, D. Li, K. Lin, Mesoporous silica beads containing active and stable tin species for the Baeyer-Villiger oxidations of cyclic ketones, Microporous Mesoporous Mater. 253 (2017) 40–48, https://doi.org/10.1016/j.micromeso.2017.06.034.
[41] E.G. Fawaz, D.A. Salam, H. Nouali, I. Deroche, S. Rigolet, B. Lebeau, T. Jean Daou, Synthesis of binderless ZK-4 zeolite microspheres at high temperature, Molecules 23 (2018) 1–13, https://doi.org/10.3390/molecules23102647.
[42] M.W. Hahn, M. Steib, A. Jentys, J.A. Lercher, Tailoring hierarchically structured SiO_2 spheres for high pressure CO_2 adsorption, J. Mater. Chem. A. 2 (2014) 13624–13634, https://doi.org/10.1039/c4ta02145b.
[43] S. Scholz, S.R. Bare, S.D. Kelly, J.A. Lercher, Controlled one-step synthesis of hierarchically structured macroscopic silica spheres, Microporous Mesoporous Mater. 146 (2011) 18–27, https://doi.org/10.1016/j.micromeso.2011.04.036.
[44] S. Scholz, J.A. Lercher, Hierarchically structured millimeter-sized (Organo) silica spheres with a macroporous shell and a meso/microporous core, Chem. Mater. 23 (2011) 2091–2099, https://doi.org/10.1021/cm1033029.
[45] L. Yu, J. Gong, C. Zeng, L. Zhang, Synthesis of monodisperse zeolite A/chitosan hybrid microspheres and binderless zeolite A microspheres, Ind. Eng. Chem. Res. 51 (2012) 2299–2308, https://doi.org/10.1021/ie202242e.
[46] D. Mehlhorn, R. Valiullin, J. Kärger, K. Schumann, A. Brandt, B. Unger, Transport enhancement in binderless zeolite X- and A-type molecular sieves revealed by PFG NMR diffusometry, Microporous Mesoporous Mater. 188 (2014) 126–132, https://doi.org/10.1016/j.micromeso.2014.01.011.
[47] K. Schumann, B. Unger, A. Brandt, G. Fischer, H. Richter, J. Jänchen, Herstellung und charakterisierung von kompakten bindemittelfreien zeolithformkörpern mit faujasit- und linde typ A-struktur, Chem.-Ing.-Tech. 86 (2014) 106–111, https://doi.org/10.1002/cite.201300026.
[48] D. Hopkins, ZK-4, (n.d.). http://www.iza-online.org/synthesis/Recipes/ZK-4.html. (Accessed 8 September 2021).
[49] R.W. Thompson, K.C. Franklin, Linde Type A, (n.d.). http://www.iza-online.org/synthesis/Recipes/Linde Type A.html. (Accessed 1 September 2021).
[50] M. Palomino, A. Corma, F. Rey, S. Valencia, New insights on CO_2-methane separation using LTA zeolites with different Si/Al ratios and a first comparison with MOFs, Langmuir 26 (2010) 1910–1917, https://doi.org/10.1021/la9026656.
[51] Y.A. Alassmy, Z. Asgar Pour, P.P. Pescarmona, Efficient and easily reusable metal-free heterogeneous catalyst beads for the conversion of CO_2 into cyclic carbonates in the presence of water as hydrogen-bond donor, ACS Sustain. Chem. Eng. 8 (2020) 7993–8003, https://doi.org/10.1021/acssuschemeng.0c02265.
[52] A. Zukal, C.O. Arean, M.R. Delgado, P. Nachtigall, A. Pulido, J. Mayerová, J. Čejka, Combined volumetric, infrared spectroscopic and theoretical investigation of CO_2 adsorption on Na-A zeolite, Microporous Mesoporous Mater. 146 (2011) 97–105, https://doi.org/10.1016/j.micromeso.2011.03.034.
[53] E. Jaramillo, M. Chandross, Adsorption of small molecules in LTA zeolites. 1. NH_3, CO_2, and H_2O in zeolite 4A, J. Phys. Chem. B 108 (2004) 20155–20159, https://doi.org/10.1021/jp048078f.